



High-sensitive and ultra-wide spectrum multifunctional triboelectric acoustic sensor for broad scenario applications[☆]

Huake Yang^{a,d}, Jun'an Lai^a, Qianying Li^a, Xuemei Zhang^a, Xiaochuan Li^a, Qianxi Yang^a, Yawen Hu^a, Yi Xi^{a,d,*}, Zhong Lin Wang^{b,c,**}

^a Department of Applied Physics, State Key Laboratory of Power Transmission Equipment & System Security and New Technology, Chongqing Key Laboratory of Soft Condensed Matter Physics and Smart Materials, Key Laboratory of Optoelectronic Technology & Systems, Chongqing University, Chongqing 400044, China

^b Beijing Institute of Nanoenergy and Nanosystems Chinese Academy of Sciences Beijing, 100083, China

^c Georgia Institute of Technology, Atlanta, GA 30332, USA

^d Chongqing Key Laboratory of Soft Condensed Matter Physics and Smart Materials, Department of Applied Physics, Analytical and Testing Center, Chongqing University, Chongqing 400044, P. R. China

ARTICLE INFO

Keywords:

Triboelectric nanogenerator
Acoustic sensor
Low sound pressure level
Ultra-wide spectrum

ABSTRACT

Based on the unique capacitance model of triboelectric technology, here, a novel self-powered triboelectric acoustic sensor (T-MIC) was fabricated, which is capable of simultaneously sensing acoustic waves not only covering the full frequency range of human hearing from 20 to 20,000 Hz, but also possessing higher frequency resolution (accuracy 1 Hz) and higher sensitivity (21.50 times) than the best reported triboelectric acoustic sensor. The T-MIC is faultless competent for commercial applications in high-quality music recording, wireless video communication, voice content inputting and human-robot interaction. Furthermore, based on the principle of acoustics, a theoretical model of T-MIC is proposed. Considering a broad selection of materials and the simpler preparation process of T-MIC, it has great advantages than that of many commercial acoustic wave sensors in performance and cost. So, the T-MIC can provide a feasible low-cost option for perception and detection of the acoustic waves in the commercial applications.

1. Introduction

With the fast development of science and technology, it is inevitable that the super smart digital city [1–3] must be formed for human society. However, the foundation of building a super intelligent and digital economy needs a cluster of Internet of Things (IoTs) [4–6] based on cloud computing that requires a very large number of sensors. Sound, as the most effective and straightforward communication channel, is an indispensable link in mobile devices, music recording, human-robot interaction and so on, which has played an essential role in building a smart city. Since the first acoustic sensor appeared in the 19th century (Carbon microphone was invented by Thomas Edison), the various acoustic sensors have been fabricated and their performances have been improved gradually as well. Among them, the electret microphone is one

of the typical acoustic sensors used widely in all kinds of acoustic detection. The polarized electret materials lead to the finite selection of the vibrating film materials, moreover, the complex fabrication process brings out the higher cost of the electret microphone. Therefore, it is necessary that the acoustic sensor need to explored further to overrides the traditional microphones. Not only that, the accurate detection of the acoustic wave is difficult, because of the wide frequency range of human hearing (from 20 to 20,000 Hz) and the low pressure in most ambient environments. Thus, the performance of the acoustic sensor needs to continue to optimize, and the higher signal-to-noise ratio, higher sensitivity, and wider frequency response of the acoustic wave sensor urgently need to be proposed to meet high-sensitivity information analysis and exchange effectively of the acoustic waves in practical IoTs application (such as wireless voice communication, real-time recording,

[☆] "Prof Zhong Lin Wang, an author on this paper, is the Editor-in-Chief of Nano Energy, but he had no involvement in the peer review process used to assess this work submitted to Nano Energy. This paper was assessed, and the corresponding peer review managed by Professor Chenguo Hu, also an Associate Editor in Nano Energy"

* Corresponding author.

** Corresponding author at: Beijing Institute of Nanoenergy and Nanosystems Chinese Academy of Sciences Beijing, 100083, China.

E-mail addresses: yxi6@cqu.edu.cn (Y. Xi), zhong.wang@mse.gatech.edu (Z.L. Wang).

human-computer interaction, etc.). At the same time, the simple manufacturing technology (cost optimization) and diversity of materials need to be considerate that is one of the key elements for realization of the huge commercial competitive advantage.

Recently, triboelectric nanogenerator (TENG) has been developed as a new electromechanical conversion technology [7–13], and its basic principle is the coupling of triboelectrification and electrostatic [14–16]. TENG has been exhibited very wide applications in mechanical sensing [17–20] and energy harvesting [21–25] due to simple structures, low cost and general materials. In particular, many acoustic wave sensors have been proposed to detect and collect the energy of the acoustic waves based on the capacitance model of TENG, such as the triboelectric acoustic energy-harvesting device [26–29] and the 3D-printed acoustic triboelectric nanogenerator [30], and the self-powered triboelectric auditory sensor based on TENG for social robotics and hearing aids (frequency range is 100–5,000 Hertz) [31] and the ultrathin eardrum-inspired self-powered acoustic sensor (frequency range is 20–5,000 Hertz) [32] and transparent and conductive nanomembranes with orthogonal silver nanowire arrays (frequency range is 100–10,000 Hertz) [33] with the best frequency response in ancient TENG work. Besides, the single fiber enables acoustic fabrics via nanometer-scale vibrations (frequency range is 20–10,000 Hertz) [34]. Although there are so many works to detect acoustic waves based on TENG, the requirements of full human hearing are still very limited thanks to the range of frequency response and the range of sound pressure level (SPL) response (most devices obtain a good output when SPL more than 100 dB). Therefore, it is urgently necessary to further develop and explore the acoustic sensors with wider frequency response and ultra-high sensitivity to detect acoustic waves accurately and achieve to meet the performance of commercial application.

To realize the full frequency response range (20–20,000 Hz) of human hearing and ultra-high sensitivity for an acoustic sensor based on TENG. Herein, the theoretical model of acoustic sensor based TENG is established and a wide frequency and high accuracy of the self-powered acoustic wave sensor based on the triboelectric capacitance of TENG (T-MIC) was demonstrated. In this self-powered sensor, the capacitance is composed of triboelectric film and metal electrode plate. The capability of this triboelectric film can be performed the integrated real-time sensing-transforming-logical response between the external acoustic waves and electrical responsivity. When it is driven by the acoustic waves, the electrical signals can be attained. Importantly, a circuit board with a triode is used to amplify the initial electrical signal of triboelectric capacitance, and an external circuit is employed to amplify and accurately detect the acoustic signals. Therefore, T-MIC can detect the full frequency range of human hearing (20–20,000 Hz) and 2.00 times than that of the best existing report [33]. Its output performance of full frequency range is much higher, especially, at a lower SPL (70 dB), the output is 21.50 times than the work [33], and its sensitivity is two times of one commercial electret microphone (sensitivity is -30 ± 3 dB). What's more, T-MIC has the potential for detecting wider frequency range (more than 20–20,000 Hz) and frequency resolution of more than 1 Hz. Moreover, not only the high output performance can be attained, but also the different materials such as FEP, PI, PET and PTFE as triboelectric films in the T-MIC can detect acoustic waves with high-sensitivity sensing and high-precision monitoring as well, while their detection sensitivity is affected by the thickness and electronegativity of the triboelectric films. These excellent properties enable T-MIC to be a highly reliable and self-powered reconfigurable in the scenes of acoustic sensor capable in high-quality music recording, real-time wireless video communication, human-robot interaction, and voice content inputting. This T-MIC can faultlessly competent the integrated real-time sensing-transforming-logic response. Beyond that, with extensive material selection and simplified process flow, T-MIC has great advantages in cost, which could provide a feasible option to reduce the cost of acoustic detection on the IoTs as well.

2. Results

2.1. Theoretical model, structure and performance of T-MIC

Figure 1A displays the simulation structure and one of the application scenarios of T-MIC. The height of T-MIC is 6 mm, the section diameter is 14 mm. A capacitance is formed of the triboelectric film and the back-metal plate under the isolation of the plastic ring. The triboelectric film is deformed by acoustic waves and the capacitance is changed, then the initial electrical signals can be generated based on the triboelectric effect. The tail structure forms a cavity which is conducive to the vibration of the film. Last, the initial electrical signals are amplified by the circuit board due to implanted a triode in T-MIC. The photograph of the detail structure is shown in fig. S1(a). Fig. 1B(I-III) show the schematic diagram of the reciprocating vibration of the film under the acoustic waves. To explore the theoretical process of electromechanical conversion for T-MIC, based on the principle of acoustic vibration and the capacitance structure of T-MIC, the movement process of the vibrated film is analyzed theoretically. First, the corresponding formula of the small amplitude wave equation in ideal fluid medium (air) is obtained

$$\nabla^2 p = \frac{1}{c^2} \frac{\partial^2 p}{\partial t^2} \quad (1)$$

Where ∇^2 is Laplace operator, p represents the sound pressure, c is the sound velocity. Get the solution of wave equation in polar coordinate system

$$p = \frac{A}{r} \exp[j(\omega t - kr)] \quad (2)$$

Where r is the distance from source point, k is the wave number (equal to ω/r), A represents the sound pressure of sound source. The detailed discussion is shown in notes S1 [35]. The sound pressure of spherical waves is diffused and varied with the increase of propagation distance. Therefore, the vibration motion state of thin film can be analyzed under the acoustic wave. The displacement variation formula of the membrane is obtained

$$u(r_1, t) = \frac{p_0}{k^2 T} \left[\frac{J_0(kr_1)}{J_0(ka)} - 1 \right] \exp(j\omega t) \quad (3)$$

Where p_0 is the peak sound pressure, T is the stretching force, J_0 presents the Bessel function, r_1 is the distance from membrane center and a is the radius of film. According to the Eq. (3), the position state diagram of the film can be obtained by programming simulation. Here, the radius of film is 5.5 mm, taking the pressure of acoustic wave (1,000 Hz) as 0.02 Pa and the stretching force as 50 N. Fig. 1B(i-iii) display the different displacement distribution in the different vibration conditions. The forward maximum displacement distribution is shown in Fig. 1B(i). The equilibrium displacement distribution is exhibited in Fig. 1B(ii), and reverse maximum unique distribution is demonstrated in Fig. 1B(iii). Fig. 1C(i) shows the distribution curve of the maximum displacement of the film. The average displacement of the film can be obtained by integration.

$$\bar{u}(t) = \frac{1}{\pi a^2} \int_0^a 2\pi u(r, t) r dr = \frac{2\pi p_0}{\pi a^2 k^2 T} \int_0^a \left[\frac{J_0(kr)}{J_0(ka)} - 1 \right] r dr \exp(j\omega t) \quad (4)$$

So, the relationship between the average displacement of the film and time is got.

$$\bar{u}(t) = \frac{p_0}{k^2 T} \frac{J_2\left(\frac{a\omega}{c}\right)}{J_0\left(\frac{a\omega}{c}\right)} \exp(j\omega t) \quad (5)$$

Where J_2 is the Bessel function. The detailed discussion is shown in notes S2. According to Eq. (5), the insert of Fig. 1C(ii) shows the simulate of the relationship between the average displacement of the film with time

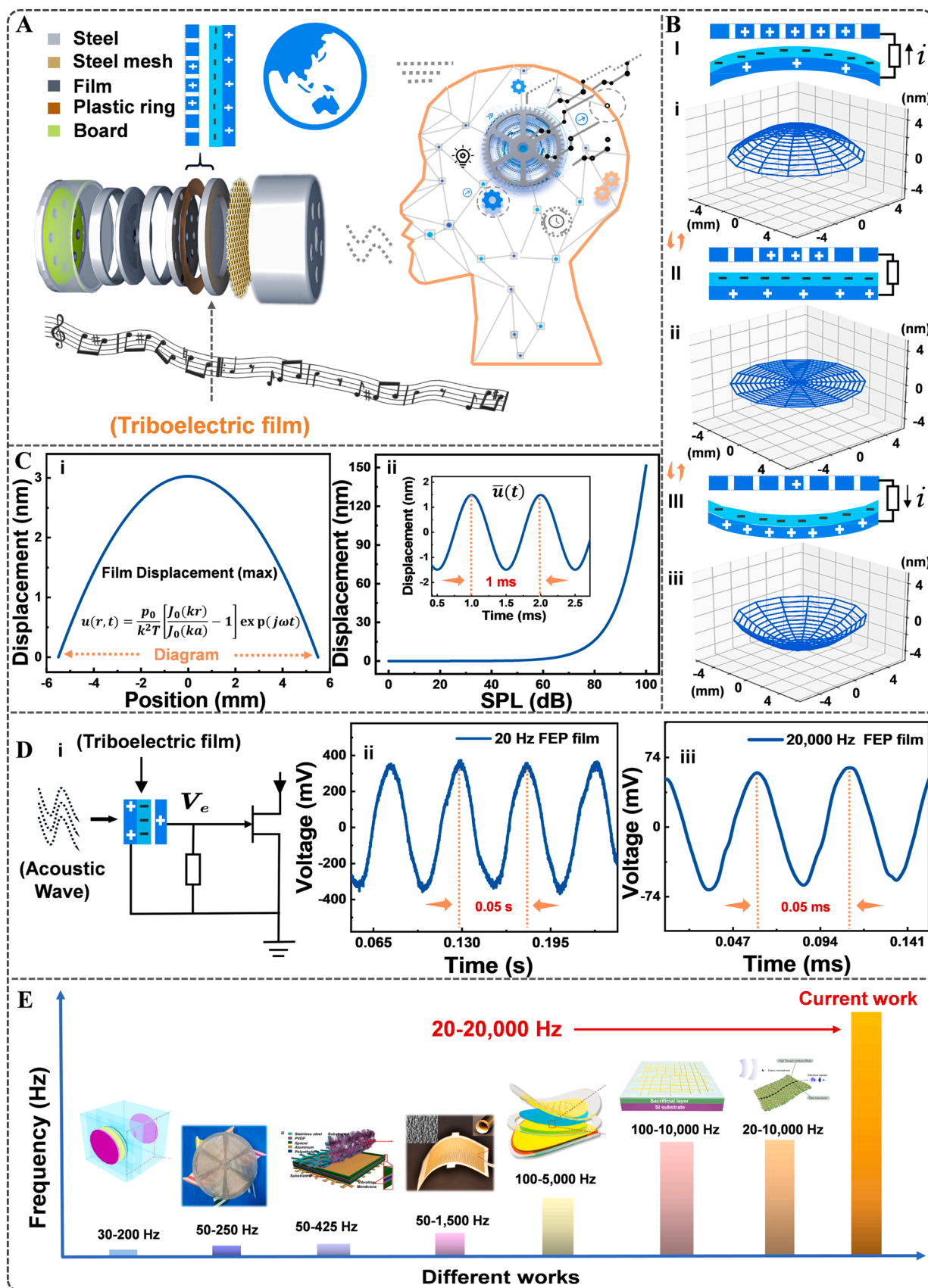


Fig. 1. Structure and mechanism of the T-MIC. (A) Structure diagram of T-MIC and the simulation scenario. (B) Charge distribution and the displacement change under the film vibration. (C) i) The maximum displacement distribution curve and ii) the relationship between displacement with SPL in simulate condition. (D) i) The equivalent circuit diagram of T-MIC, ii) and iii) the waveforms at frequencies of 20 and 20,000 Hz detected by FEP film. (E) The comparison for reported TENG acoustic sensors with T-MIC.

in simulate condition. From the simulation results, the frequency of the average changed displacement is 1000 Hz. The calculation formula of SPL with sound pressure is

$$SPL = 20lg \frac{P_e}{P_{rfe}} \quad (6)$$

Where p_e is the measured effective value of the sound pressure. p_{rfe} is the reference sound pressure and $p_{rfe} = 2 \times 10^{-5}$ Pa in the air. The relationship between SPL and sound pressure is shown in Fig. S1(b). Based on Eqs. (5) and (6), therefore, the relationship between average displacement $\bar{u}(t)$ and SPL can be simulated as shown in Fig. 1C(ii), and the displacement increase exponentially with SPL. Under extreme SPL or other interference, the film can contact the metal plate (fig. S2(a)). Due to the difference of electron affinity, it also can generate triboelectric charges. Fig. S2(b) displays schematic diagram of triboelectric charge generating for four states. When atoms are close to each other, electron clouds are overlap, and the electrons move from the high-energy to low-energy levels, and generate stable transferred charges. Two sides of FEP film after evaporating in fig. S2(c) and the simulation curve for output voltage of higher SPL in fig. S2(d). Fig. 1D(i) illustrates the equivalent circuit diagram of the T-MIC. Triboelectric film is deformed by acoustic

waves and the capacitance of the T-MIC is changed, so the original signals are generated in external circuit and amplified by the triode. The amplification curves of the whole circuit with different frequency signals are shown in fig. S2(e). Fig. 1D(ii, iii) plot the waveforms of 20 and 20,000 Hz acoustic waves detected by T-MIC (FEP film, 30 μ m), which shows a great wide frequency response range. Fig. 1E shows the comparison of T-MIC with the representative previous works of acoustic sensors based on TENG. As from results, this work is much higher than the previous works in detecting the frequency range of acoustic waves.

2.2. Performance with materials and thickness

The property of the different materials as triboelectric film materials and the different thicknesses for the same triboelectric material is investigated. Fig. 2 presents the high-accuracy output performance of the FEP triboelectric film (Unless otherwise specified, the applied triboelectric film thickness is 30 μ m.) under the different SPL and different frequency acoustic waves. fig. S2(c) shows the photographs of the front and back of the FEP film after being stuck with metal ring. A layer of copper (400 \AA) has evaporated on the surface. The size scheme after evaporation is illustrated in Fig. 2A(i), where D (11 mm) is the effective diameter of the film, d_1 (30 μ m) is the thickness of film, d_2

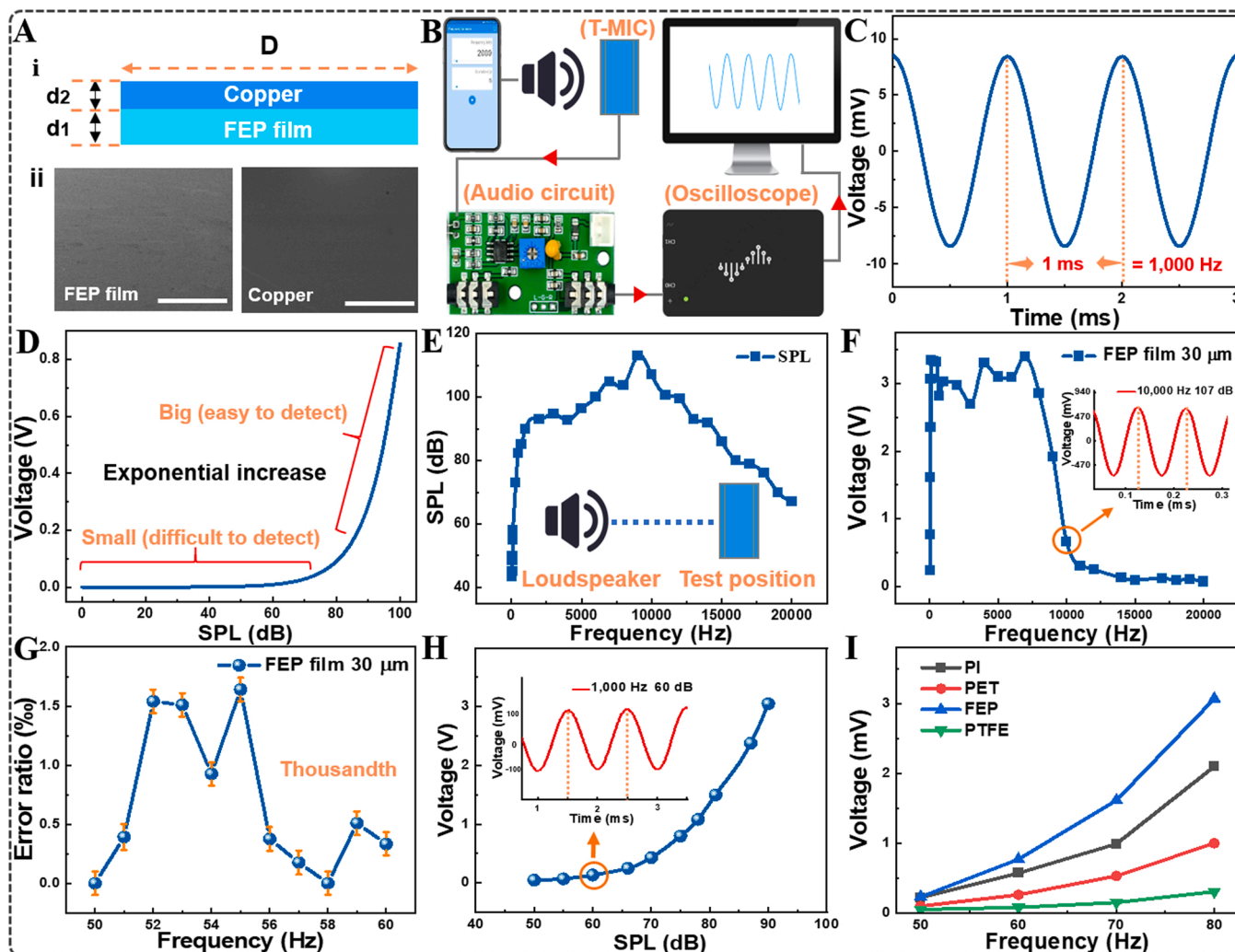


Fig. 2. The output of FEP film under different frequency acoustic waves. (A) i) Schematic illustration for film size, ii) SEM pictures of FEP film before and after evaporating copper (scale bar, 10 μ m). (B) Schematic illustration of measure process. (C) The theoretical simulation relationship between output voltage with time in simulate condition. (D) The simulation curve for output voltage and SPL. (E) The SPL of different frequency acoustic waves in the same test position. (F) Output voltage with different frequency acoustic waves. (G) Detected frequency accuracy of T-MIC with FEP film (30 μ m). (H) The output voltage of T-MIC under different SPL (1000 Hz). (I) Output voltage of different triboelectric films under low frequency acoustic waves (50, 60, 70 and 80 Hz).

(400 Å) is the thickness of copper layer. The SEM pictures also show the surface before and after evaporating copper (Fig. 2A(ii)). The schematic diagram of measure process is shown in Fig. 2B. Unless otherwise specified, the applied acoustic waves are generated by a mobile phone (50–20,000 Hz), then the signal of device is transmitted to the amplification circuit board and displayed in the computer by an oscilloscope. When the film is vibrated by acoustic waves, the output voltage generated by the average displacement is

$$e = \frac{4\pi k_0 \sigma}{\epsilon_r} \bar{u}(t) \quad (7)$$

Where k_0 is the Electrostatic constant, σ is the change density of triboelectric charge, ϵ_r is the relative dielectric constant. According to the Eq. (5), the output voltage of capacity of film with metal plate is

$$e = \frac{4\pi k_0 \sigma p_0}{\epsilon_r k^2 T} \frac{J_2\left(\frac{\omega a}{c}\right)}{J_0\left(\frac{\omega a}{c}\right)} \exp(j\omega t) \quad (8)$$

The detailed discussion is shown in notes S3. The relative dielectric constant of air $\epsilon_r = 1$ and the density of triboelectric charge $\sigma = 50 \mu\text{C}/\text{m}^2$ were taken in the simulation conditions of Fig. 1C. The theoretical simulation relationship between output voltage and time is shown in Fig. 2C. From the theoretical simulation, the output frequency is the same as that of the input acoustic wave. According to Eqs. (6) and (8), the simulation relationship curve between output voltage with SPL is obtained and the output voltage increase exponentially with SPL, as displayed in Fig. 2D, indicating that it's easy to had an output in higher SPL. Fig. 2E plots the SPL of testing position. It shows that under the same setting conditions of loudspeaker, the changed frequency of the input electrical signal, thus, the loudspeaker emits sound waves of corresponding frequencies respectively. A certain location is selected to measure the SPL with a decibel meter and the performance of T-MIC. Therefore, each data in Fig. 2E represents the SPL with different emitted frequencies by the loudspeaker at the same location. The frequencies are from 50 to 20,000 Hz and the range of SPL is from 43.5 dB to 113 dB. Fig. 2F presents the voltage signals of the FEP triboelectric film with different frequencies at the testing position, and the inset shows the waveform of acoustic wave of 10,000 Hz. In particular, the range of output voltage is 69–3400 mV, indicating that the output characteristics shows each frequency acoustic waves can be detected by T-MIC. Figs. S3 (a, b) and 1D(ii) also display the waveforms of acoustic waves with the frequencies of 30, 40 and 20 Hz under the high-power loudspeaker. Unless otherwise specified, the applied acoustic waves are 20, 30 and 40 Hz under the high-power loudspeaker. Figs. S3(c-o) and fig. S4(a-f) show the waveforms of other frequency acoustic waves. Indicating that this T-MIC simultaneously possesses the full frequency range of human hearing and high sensitivity and the great stability. This device can still maintain 95.4% of the output performance after 60 days (Fig. S4 (g)). The comparison of bottom noise signal and standard acoustic signal (1000 Hz, 90 dB) are shown in Fig. S4(h). The output performance for continuous working 48 h is displayed in Fig. S4(i), which shows the output property is little attenuation. The frequency accuracy is one of important parameter for acoustic sensor. Therefore, the detected frequency accuracy of T-MIC was explored as well (Fig. 2G). An interval of 1 Hz with the acoustic waveforms of 50–60 Hz (generated by the high-power loudspeaker) can be distinguished accurately by FEP film T-MIC, the error ratio is less than 1.64% and the waveforms are shown in Figs. S5(a-k). Meanwhile, Figure S6 displays the smooth response curve of T-MIC at range of frequencies 20–22,000 Hz. These results show T-MIC possesses the potential for being up to wider frequency detection range and frequency resolution of more than 1 Hz. The output voltage of the device with 1000 Hz at different SPL is shown in Fig. 2H. As seen from Fig. 2H, when increasing the SPL, the output voltage is increased exponentially. The results are according with the theoretical model results of the Fig. 2D and Eq. (8). According to the results of FEP

triboelectric film, this T-MIC faultless competent to detect the acoustic waves with ultra-high precision and ultra-wide frequency response range as well. Such good performance of this T-MIC may benefit from commercial applications.

To illustrate the universality of triboelectric films can be used in this T-MIC, PI, PET and PTFE films also are employed as triboelectric films of T-MIC, and the corresponding properties were also investigated. Fig. S7 presents Fourier infrared spectrum of FEP, PI, PET and PTFE film respectively. Fig. S8 exhibits the output performance of PI film. Fig. S8 (a) plots the SPL of the testing position (50–20,000 Hz). Fig. S8(b) shows the output voltage of PI triboelectric film under the different frequency acoustic waves (50–20,000 Hz), and the range of output voltage is 66.5–3210 mV. The output waveforms of different frequency acoustic waves are shown in Fig. S9. Figures S9(a-c) exhibit the waveforms of acoustic waves (20, 30 and 40 Hz), other frequency waveforms are displayed in figs. S9(d-o). As a result, PI film as triboelectric material of T-MIC can be well realizing the goal of the wider frequency and high sensitivity. Similar characteristics can be attained for PET and PTFE film. Figure S10 exhibits the output performance of PET film. Figure S10 (a) displays the SPL at testing position. The output voltage (98–3400 mV) of PET triboelectric film is shown in fig. S10(b). Figure S11 exhibits the output waveforms of PET triboelectric film (including the waveforms of 20, 30 and 40 Hz). As a result, PET film also can be well realizing the goal of the wider frequency and high sensitivity. Figure S12 shows the SPL of testing position and the output of PTFE triboelectric film, and the range of output voltage is 50–3080 mV. The output waveforms are displayed in fig. S13 (including the waveforms of 20, 30 and 40 Hz). In addition, the comparison of the output performance for the different triboelectric materials are observed under low frequencies (50–80 Hz) with the same SPL (Fig. 2I), which is consistent with the output of the triboelectric electronegativity sequence table except for PTFE. The roughness and flatness of PTFE triboelectric film, i.e., dents on the surface, result in the output fluctuation, further confirming by the SEM image of PTFE triboelectric film shown in fig. S14. Thus, Fig. 2I indicates the output performance is larger with higher electronegativity (equal to surface charge density), which the results further verify Eq. (8). These materials all as triboelectric material for T-MIC exhibit high sensitivity and high precision, thus satisfying the requirement of detection acoustic waves. So many organic thin-films can be employed as triboelectric materials of this T-MIC. Compared with electret materials of electret acoustic sensors, triboelectric materials are cheaper and simpler in process requirements (especially without high-voltage polarization equipment). Therefore, it uses the general triboelectric materials as the vibration film of acoustic sensors instead, which can further lower the cost consumption.

In addition, given the excellent property of the device, the applied different thickness influence for thin-film is worthy of investigation for acoustic wave detection. Theoretically, the more thickness film is obtained the more stretching force. Thus, the thickness of film is proportional to the stretching force, while the output property is inversely proportional to the stretching force, according to Eq. (8). The thicknesses of PI triboelectric films are selected with 9 μm , 12.5 μm , 30 μm , 50 μm and 75 μm . A layer of the copper electrode (400 Å) was fabricated on the surface of each film by evaporation respectively. Figures S15(a-e) show the SPL with the testing position in different thickness films (50–20,000 Hz) respectively. Figures S16(a-e) show the output voltage of PI triboelectric films with different thicknesses respectively. Figure S16(f) plots the comparison of the output at the frequencies from 50 to 80 Hz with the same SPL. From the results, it can be concluded that the increased the output voltage with the decreased the stretching force gradually, conforming to Eq. (8). Meanwhile, the thinner material possesses the better output property.

2.3. Comparison of triboelectric charge with traditional electret charge

The electret polymer film is widely used in traditional electret

acoustic sensors, and the charges on the surface of electret polymer film can be generated from the polarization of the materials, that is say, the charge on the surface is polarized charge for the electret polymer film. During the manufacturing and working electret polymer film, however, the fiction and vibration are inevitable, and the triboelectric charge may be generated if the electret polymer film as the triboelectric film. It should confirm whether the surface charges of electret film could contain the triboelectric charges, so two experiments are designed in Fig. 3A. Based on the electrostatic induction, the output voltages under three conditions (static, vibrated by air flow and rub with metal) were detected to verify the triboelectric effect in piezoelectric electret PVDF film shown in Fig. 3A(i). The second experiment was designed to confirm whether the triboelectric changes can be ignored in different acoustic sensors in Fig. 3A(ii). The first verified method is used non-contact model (Fig. 3B). The electret PVDF film (diameter, 50 mm) is fixed at position x_1 and the metal electrode is driven by the linear motor to make a reciprocating motion between x_2 and x_3 ($d_1 = 3.7$ mm, $d_2 = 40$ mm). To eliminate the electrostatic induced charges and other small particles, the original piezoelectric electret film was cleaned by alcohol. Fig. 3C shows the output voltage of the original electret PVDF film, which is almost 0 V and makes almost no charge in the non-contact

model for device. As from seen Fig. 3D, when the electret PVDF film was vibrated by air gun (supplementary movies 1), the output voltage is about 0.7 V in the same model for device. While the electret PVDF film was rubbed with a metal, the output voltage is about 15 V under the same model, as displayed in Fig. 3E. As a result, the output voltage of the rubbed piezoelectric electret PVDF film makes noticeable improvement and is much higher than others obviously. It is proved that triboelectric changes can be generated by a piezoelectric electret PVDF film. To further verify it, A pure PVDF film ($8 \mu\text{m}$, unpolarized) and an electret PVDF film were applied for comparison with a commercial electret microphone (diameter, 14 mm; thickness, 7 mm). Fig. 3(F-H) exhibit the voltage output of T-MIC (pure PVDF film and piezoelectric electret PVDF film) and a commercial piezoelectric electret microphone possessing same size of device in 50–20,000 Hz frequencies, the corresponding SPL are shown in figs. S17 (a-c), respectively. As from results, the output voltage of polarized electret PVDF film is the largest among three devices, likewise, the output voltage of rubbed pure PVDF film cannot be ignored. Fig. 3I shows the output comparison of three sensors from 50 to 80 Hz, indicating further that the triboelectric charges are possessed when the working polymer film was rubbed after. In addition, supplementary movies 2 shows the working of T-MIC that triboelectric charge

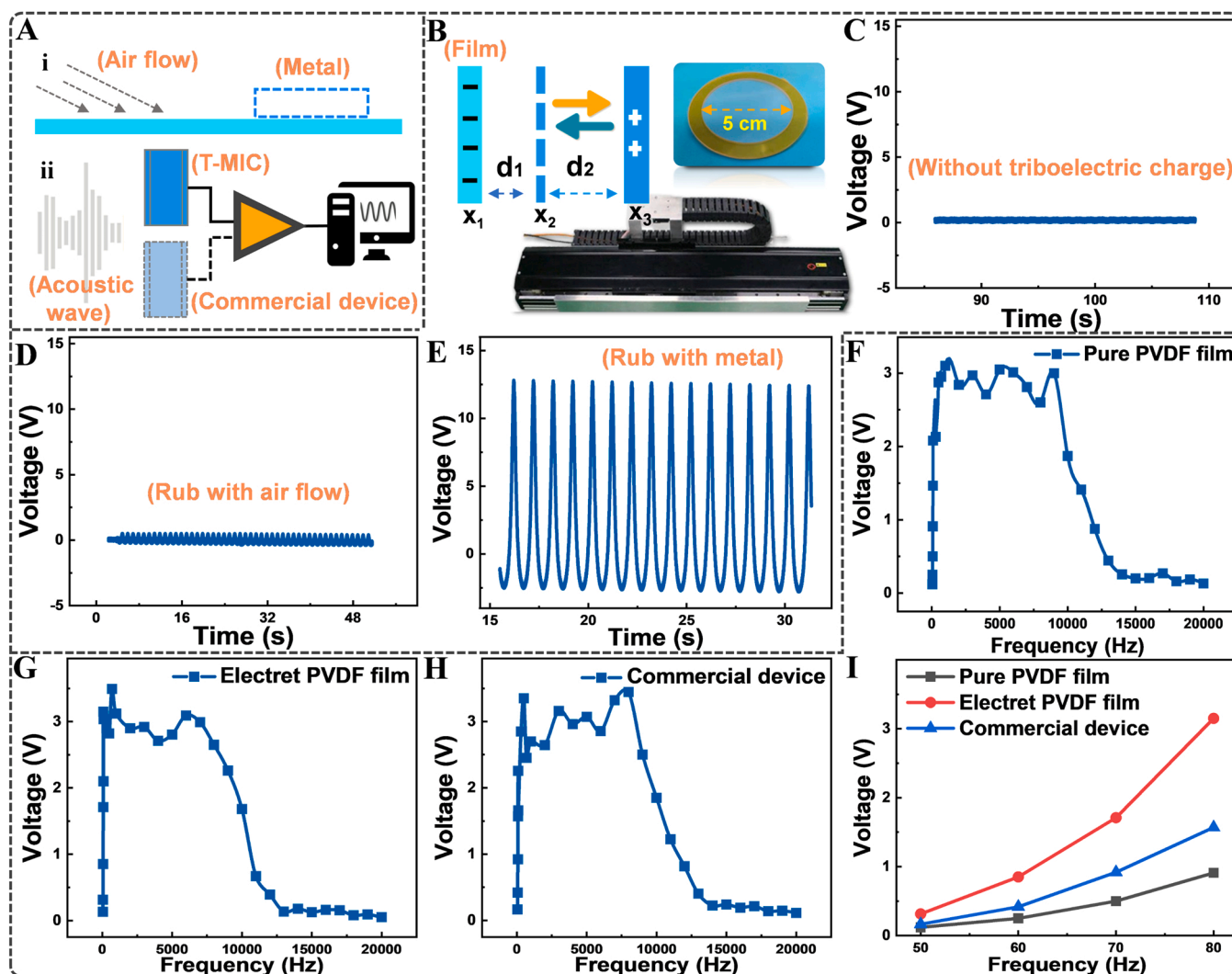


Fig. 3. The influence of triboelectric effect on traditional polymer electret acoustic sensor. (A) Schematic illustration of two verifying methods. (B) Schematic measurement illustration of non-contact model. (C) Output voltage of the original piezoelectric electret PVDF film. (D) Output voltage of piezoelectric electret PVDF film vibrated by high-pressure air flow. (E) Output voltage of piezoelectric electret PVDF film after rubbing with metal. (F) Output voltage of T-MIC with a pure PVDF film. (G) Output voltage of T-MIC with a piezoelectric electret PVDF film. (H) Output voltage of a commercial electret microphone. (I) Comparison the output voltage of three devices (pure PVDF film, piezoelectric electret PVDF film and commercial device) under the same acoustic waves (50–80 Hz).

signal was attained on the surface of the PI film after being cleaned with alcohol. In a word, it can be concluded that the electret polymer film also has the triboelectric effect and the influence of triboelectric charge need to be considered in the traditional electret acoustic sensors.

Supplementary material related to this article can be found online at [doi:10.1016/j.nanoen.2022.107932](https://doi.org/10.1016/j.nanoen.2022.107932).

2.4. Excellent acoustic detection and human-robot interaction system

Driven by the rapidly increasing demand of global markets, acoustic sensors are widely used for music recording, wireless communication, human-robot interaction, and so on. Benefiting from the working mechanism and structure, our T-MIC simultaneously possesses high sensitivity and wide broadband response covering the full range of human hearing (20–20,000 Hz). Our T-MIC with high performance promises as a superior acoustic sensor. To demonstrate it, the T-MIC and a commercial electret microphone (sensitivity, -30 ± 3 dB, fig. S18) were used to record the same music, respectively. Fig. 4A shows the schematic diagram of the recording process. The T-MIC is installed in a metal shielding shell to reduce the environmental electromagnetic interference, the signal is recorded on computer by an audio circuit board which is disassembled from the same commercial electret microphone (fig. S19). Fig. 4B shows the photograph of recording music with T-MIC and the scale bar is 10 cm. Fig. 4C plots the curve of real-time SPL at the position when recording a famous classic music (Serenade-Wolfgang Amadeus Mozart). The SPL distributes in 50–70 dB mainly. Fig. 4(D–F) show the output acoustic spectrum diagram of FEP

film (supplementary audio 1), commercial electret microphone (supplementary audio 2) and PI film (supplementary audio 3), respectively. It can be found that the output of T-MIC (the upper part of Fig. 4(D–F)) is better than that of the commercial electret microphone. Especially, the output signals of FEP film are twice higher than the commercial electret microphone. The acoustic spectrum diagram of three devices are shown in the bottom of Fig. 4(D–F). Two corresponding frequency bands are marked by white dash lines (10,000 Hz and 20,000 Hz), confirming that our T-MIC can retain more details than that of the commercial electret microphone. Especially, in the frame area of the dashed line, our T-MIC has a better capability to record high-frequency acoustic waves (10,000–20,000 Hz). In the quality of hearing, the recorded music of T-MIC is also better than this commercial electret microphone. The supplementary audio (4, 5) are recorded by PET and PTFE film of the T-MIC. To demonstrate the excellent performance of T-MIC further, the same song is recorded with lower SPL (FEP film, supplementary audio 6) in Fig. 4(G, H). The SPL is distributed in 40–60 dB mainly, and the spectrum diagram shows T-MIC also has a great performance with low SPL. Besides, if have a better loudspeaker and recording environment, the recording quality of T-MIC might be much better. Therefore, our T-MIC has excellent performance so that it is further applied to implement the real-time sound sensing-transforming-logical response processing functionalities for many work scenarios. Not only that, our T-MIC (FEP film) is applied for a wireless video communication system directly shown in Fig. 4I. The realistic scene picture shows two users taking real-time wireless video communication on the computer through T-MIC, as shown in supplementary movies 3.

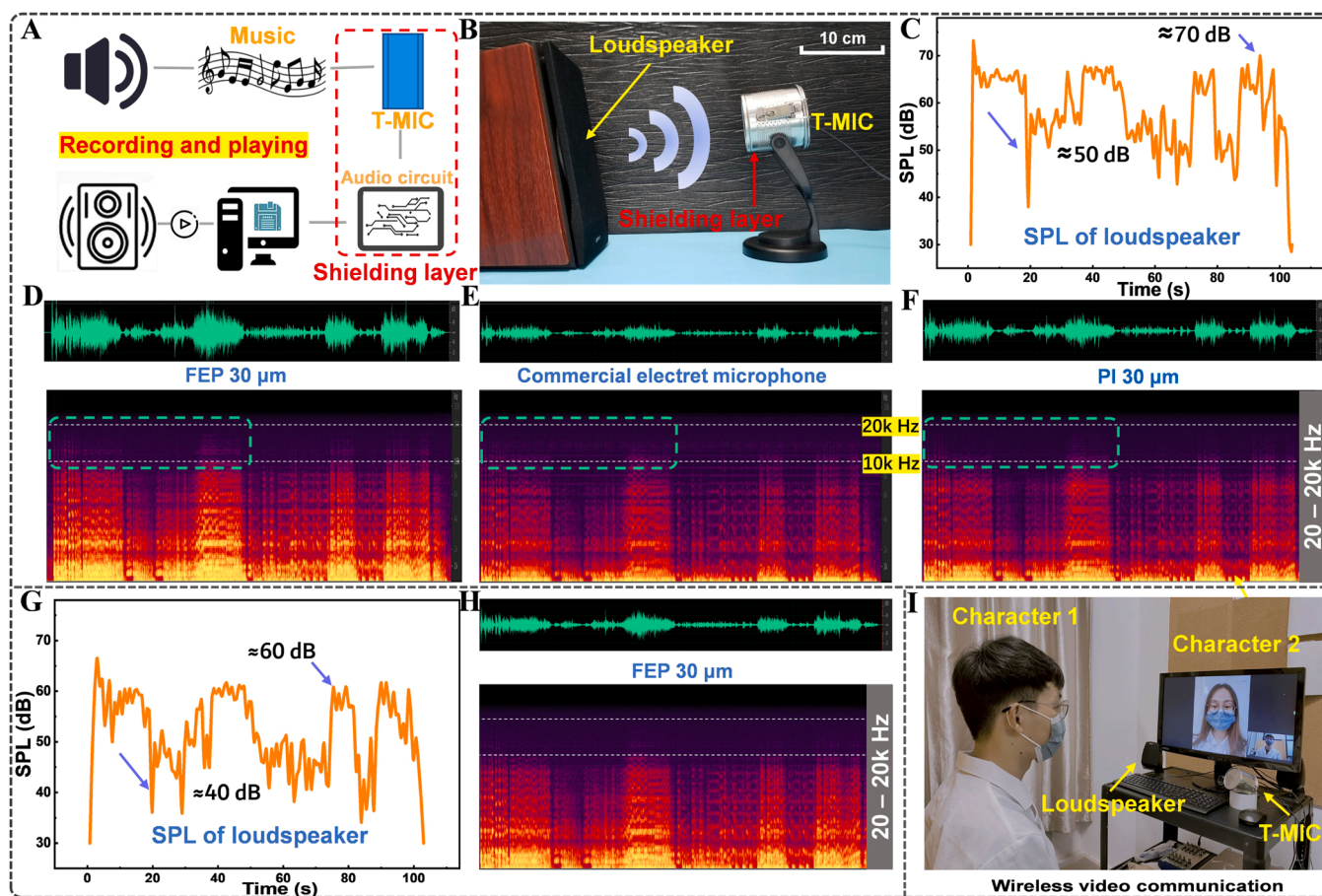


Fig. 4. Practical applications of T-MIC in high-quality music recording and wireless video communication. (A) Schematic illustration of music recording process. (B) The photograph of music recording with T-MIC. (C) The SPL curve of music at the recording position. The recorded music spectrum diagram by PET film T-MIC (30 μm) (D), a commercial microphone (E) and PI film T-MIC (30 μm) (F), respectively. (G) The SPL curve at music recording position (lower SPL). (H) The recorded music spectrum diagram for FEP film T-MIC under lower SPL. (I) FEP film T-MIC for a wireless video communication system.

Supplementary material related to this article can be found online at [doi:10.1016/j.nanoen.2022.107932](https://doi.org/10.1016/j.nanoen.2022.107932).

In addition, the integrated real-time sensing-transforming-logic response functionalities of our T-MIC can be realized. Fig. 5 presents the application of voice control of robot and voice inputting based on our T-MIC. The schematic illustrations of human-robot interaction were proposed in Fig. 5A. Prior to realization it, the original commercial microphone of the robot is removed and replaced by our T-MIC. As photograph shown in Fig. 5B, our T-MIC was employed as voice controls in the practical application, and T-MIC (FEP, 30 μm) is installed on the back of the robot (top of Fig. 5B) and electromagnetic and other environmental interference is shielded by a metal shell. Fig. 5C shows the voice recorded from a person saying “Go forward”, realizing human-robot interaction of voice control between a robot and T-MIC and the integrated real-time sensing-transforming-logic response functionalities of T-MIC. More voice commands and robot responses are also shown in the supplementary movies 4 and 5, confirming further the integrated real-time sensing-transforming-logic response functionalities of T-MIC as well. Not only that, the photograph of conversion of voice content to text is realized on the computer using T-MIC, as illustrated in Fig. 5D. Fig. 5(E, F) also reveal the original voice signals and spectrum diagram of the master’s speech whose content is “Hello, it’s a nice day” (supplementary movies 6). The experimental results indicate that T-MIC can always record the content of people’s voices completely and correctly, indicating that our can meet with the integrated real-time sensing-transforming-logic response functionalities. So, this T-MIC can faultlessly competent the integrated real-time sensing-transforming-logic response functionalities. Moreover, the high sensitivity and wide spectrum and zero energy consumption are prospected for T-MIC. In conclusion, T-MIC with excellent performance and lower comprehensive cost, underscoring its potential in the acoustic sensor industry.

Supplementary material related to this article can be found online at [doi:10.1016/j.nanoen.2022.107932](https://doi.org/10.1016/j.nanoen.2022.107932).

3. Discussion

In summary, we demonstrate an integrated of sensing-transforming-logic response and high property T-MIC acoustic wave sensor. Benefiting from the excellent designed, this T-MIC is the best TENG-based acoustic sensor so far, and it not only possesses the wider frequency response range with the full frequency of human beings (20–20,000 Hz), but also the output voltage is much higher, especially, at a lower SPL 70 dB, 21.5 times than that of other acoustic sensors based TENG. Some common triboelectric materials can be used in triboelectric materials of T-MIC acoustic waves as well, as the results, the thinner material has the better output property. Meanwhile, the triboelectric charges can be generated in the rubbed electret film of the traditional electret acoustic wave sensors. Using the T-MIC as acoustic wave sensor, the T-MIC exhibited the capability to perform in high-quality music recording. The T-MIC was further demonstrated with an integrated of sensing-transforming-logic response, including wireless video communication, constructing an electronic auditory system and voice input. Moreover, T-MIC has the potential for detecting wider frequency range and frequency resolution of more than 1 Hz. With these capabilities, this study might bring a way for the technical, process and cost optimization for the acoustic sensor industry and a feasible option to reduce the cost of acoustic detection in the IoTs.

4. Materials and methods

4.1. T-MIC fabrication

T-MIC is mainly divided into ten parts. First, to shield electromagnetic interference, a metal shell (diameter, 14 mm; inner diameter, 13 mm; height, 6 mm) is employed as Faraday cage, and several channels in cross-section send the acoustic wave. Metal mesh (diameter, 13 mm; thickness, 0.5 mm) also regard as shielding interference layer.

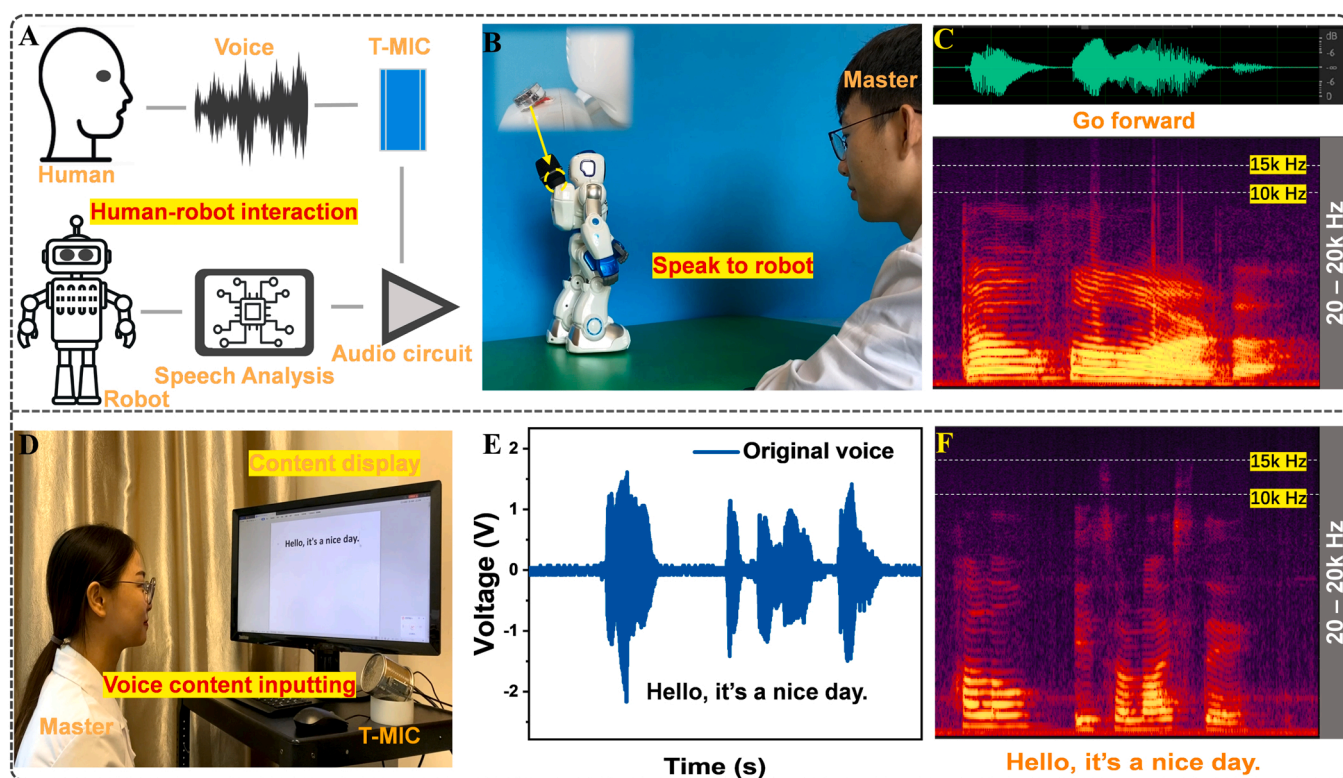


Fig. 5. Applications of T-MIC in human-robot interaction and voice content inputting. (A) Schematic illustration of human-robot interaction. (B) The real photograph of a master gives voice commands to the robot. (C) Acoustic wave information of a voice command. (D) The real photograph of voice content inputting. (E) The original voice signals. (F) Detail information of voice signals.

One side is plated with copper (400 Å) of the triboelectric film (diameter, 13 mm; thickness, varied) which sticks on a metal ring (outer diameter, 13 mm; inner diameter, 11 mm; thickness, 1 mm). So, the effective diameter of the triboelectric film is 11 mm. Plastic ring (outer diameter, 13 mm; inner diameter, 11 mm; thickness, 150 μm) is used the gap between film and metal plate. The metal plate (diameter, 12 mm; thickness, 0.75 mm) with several channels are used as the part of capacitor. So, when the triboelectric film is driven by the acoustic wave and the electrical signals can be attained. Under the electrode metal plate, there is a metal ring (outer diameter, 12 mm; inner diameter, 11 mm; thickness, 1.2 mm). The metal plate (diameter, 12 mm; thickness, 0.48 mm) with a channel and another metal ring (outer diameter, 12 mm; inner diameter, 11 mm; thickness, 1.5 mm) are formed the rear cavity. These two metal plates and two metal rings are wrapped by a plastic ring (outer diameter, 13 mm; inner diameter, 12 mm; height, 4 mm) in order to prevent causing a short circuit with the metal shell. The last one is a circuit board (diameter, 13 mm; thickness, 1 mm) which integrated with a triode to amplify the electrode signal of the capacitor and two output electrodes are led out on the back.

Funding

National Key R & D Project from Minister of Science and Technology (2021YFA1201602), National Natural Science Foundation of Chongqing (cstc2019jcyj-msxmX0068), National Natural Science Foundation of China (NSFC) (52272191, U21A20147, 52073037), Fundamental Research Funds for the Central Universities (Grant No. 2021CDJQY-005).

CRedit authorship contribution statement

Huake Yang, Yi Xi, Zhong Lin Wang: Conceptualization, Methodology, Software, Writing – review & editing. **Huake Yang, Jun'an Lai, Qianying Li:** Data curation, Writing – original draft preparation. **Qianxi Yang, Yawen Hu:** Visualization, Investigation. **Yi Xi:** Supervision. **Jun'an Lai, Xuemei Zhang, Xiaochuan Li:** Software, Validation. **Huake Yang, Yi Xi, Xuemei Zhang, Zhong Lin Wang:** Writing – review & editing. .

Data and materials availability

All data needed to evaluate the conclusions in the paper are present in the paper and/or the Supplementary Materials. Additional data related to this paper may be requested from the authors.

Declaration of Competing Interest

The authors declare that they have no known competing financial interests or personal relationships that could have appeared to influence the work reported in this paper.

Data availability

Data will be made available on request.

Acknowledgments

We thank Analytical and Testing Center of Chongqing University for some electrode preparations and material characterizations.

Appendix A. Supporting information

Supplementary data associated with this article can be found in the online version at [doi:10.1016/j.nanoen.2022.107932](https://doi.org/10.1016/j.nanoen.2022.107932).

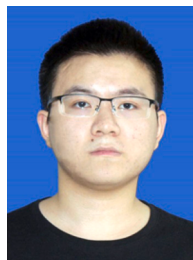
References

- [1] E. Ismagilova, L. Hughes, Y.K. Dwivedi, K.R. Raman, Smart cities: advances in research-An information systems perspective, *Int. J. Inf. Manag.* 47 (2019) 88–100, <https://doi.org/10.1016/j.ijinfomgt.2019.01.004>.
- [2] R. Napolitano, W. Reinhart, J.P. Gevaudan, Smart cities built with smart materials, *Science* 371 (2021) 1200–1201, <https://doi.org/10.1126/science.abg4254>.
- [3] A. Ramaswami, A.G. Russell, P.J. Culligan, K.R. Sharma, E. Kumar, Meta-principles for developing smart, sustainable, and healthy cities, *Science* 352 (2016) 940–943, <https://doi.org/10.1126/science.aaf7160>.
- [4] E. Hittinger, P. Jaramillo, Internet of Things: Energy boon or bane? *Science* 364 (2019) 326–328, <https://doi.org/10.1126/science.aau8825>.
- [5] J.J. Luo, W.C. Gao, Z.L. Wang, The triboelectric nanogenerator as an innovative technology toward intelligent sports, *Adv. Mater.* 33 (2021), <https://doi.org/10.1002/adma.202004178>.
- [6] X. Zhao, H. Askari, J. Chen, Nanogenerators for smart cities in the era of 5G and Internet of Things, *Joule* 5 (2021) 1391–1431, <https://doi.org/10.1016/j.joule.2021.03.013>.
- [7] J. Chen, Z.L. Wang, Reviving vibration energy harvesting and self-powered sensing by a triboelectric nanogenerator, *Joule* 1 (2017) 480–521, <https://doi.org/10.1016/j.joule.2017.09.004>.
- [8] Z.L. Wang, Triboelectric Nanogenerator (TENG)-Sparking an Energy and Sensor Revolution, *Adv. Energy Mater.* 10 (2020), <https://doi.org/10.1002/aem.202000137>.
- [9] C. Chen, et al., 3D double-faced interlock fabric triboelectric nanogenerator for bio-motion energy harvesting and as self-powered stretching and 3D tactile sensors, *Mater. Today* 32 (2020) 84–93, <https://doi.org/10.1016/j.mattod.2019.10.025>.
- [10] K. Dong, X. Peng, Z.L. Wang, Fiber/fabric-based piezoelectric and triboelectric nanogenerators for flexible/stretchable and wearable electronics and artificial intelligence, *Adv. Mater.* 32 (2020), <https://doi.org/10.1002/adma.201902549>.
- [11] T. Jin, et al., Triboelectric nanogenerator sensors for soft robotics aiming at digital twin applications, *Nat. Commun.* 11 (2020), <https://doi.org/10.1038/s41467-020-19059-3>.
- [12] D. Liu, et al., A constant current triboelectric nanogenerator arising from electrostatic breakdown, *Sci. Adv.* 5 (2019), <https://doi.org/10.1126/sciadv.aav6437>.
- [13] Z.L. Wang, On the first principle theory of nanogenerators from Maxwell's equations, *Nano Energy* 68 (2020), 104272, <https://doi.org/10.1016/j.nanoen.2019.104272>.
- [14] Q. Zheng, et al., In Vivo Powering of Pacemaker by Breathing-Driven Implanted Triboelectric Nanogenerator, *Adv. Mater.* 26 (2014) 5851–5856, <https://doi.org/10.1002/adma.201402064>.
- [15] Q. Zheng, et al., Biodegradable triboelectric nanogenerator as a life-time designed implantable power source, *Sci. Adv.* 2 (2016), <https://doi.org/10.1126/sciadv.1501478>.
- [16] Y. Zou, et al., A bionic stretchable nanogenerator for underwater sensing and energy harvesting, *Nat. Commun.* 10 (2019), <https://doi.org/10.1038/s41467-019-10433-4>.
- [17] J. Nie, et al., Power generation from the interaction of a liquid droplet and a liquid membrane, *Nat. Commun.* 10 (2019), <https://doi.org/10.1038/s41467-019-10232-x>.
- [18] H. Ouyang, et al., Symbiotic cardiac pacemaker, *Nat. Commun.* 10 (2019), <https://doi.org/10.1038/s41467-019-09851-1>.
- [19] Z. Wang, et al., Ultrahigh electricity generation from low-frequency mechanical energy by efficient energy management, *Joule* 5 (2021) 441–455, <https://doi.org/10.1016/j.joule.2020.12.023>.
- [20] J. Xiong, et al., Skin-touch-actuated textile-based triboelectric nanogenerator with black phosphorus for durable biomechanical energy harvesting, *Nat. Commun.* 9 (2018), <https://doi.org/10.1038/s41467-018-06759-0>.
- [21] C. Chen, et al., Micro triboelectric ultrasonic device for acoustic energy transfer and signal communication, *Nat. Commun.* 11 (2020), <https://doi.org/10.1038/s41467-020-17842-w>.
- [22] X. Fan, et al., Ultrathin, rollable, paper-based triboelectric nanogenerator for acoustic energy harvesting and self-powered sound recording, *ACS Nano* 9 (2015) 4236–4243, <https://doi.org/10.1021/acsnano.5b00618>.
- [23] R. Hinchet, et al., Transcutaneous ultrasound energy harvesting using capacitive triboelectric technology, 491+, *Science* 365 (2019) <https://doi.org/10.1126/science.aan3997>.
- [24] W.H. Xu, et al., A droplet-based electricity generator with high instantaneous power density, 392+, *Nature* 578 (2020) <https://doi.org/10.1038/s41586-020-1985-6>.
- [25] Yu, H.Y. et al. in 16th IEEE International Conference on Nano/Micro Engineered and Molecular Systems (IEEE-NEMS). 1676–1679 (2021).
- [26] J. Chun, et al., Mesoporous pores impregnated with Au nanoparticles as effective dielectrics for enhancing triboelectric nanogenerator performance in harsh environments, *Energy Environ. Sci.* 8 (2015) 3006–3012, <https://doi.org/10.1039/c5ee01705j>.
- [27] K. Dong, et al., Shape adaptable and highly resilient 3D braided triboelectric nanogenerators as e-textiles for power and sensing, *Nat. Commun.* 11 (2020), <https://doi.org/10.1038/s41467-020-16642-6>.
- [28] Y. Song, et al., Wireless battery-free wearable sweat sensor powered by human motion, *Sci. Adv.* 6 (2020), <https://doi.org/10.1126/sciadv.aay9842>.
- [29] R.Y. Zhang, et al., Cellulose-based fully green triboelectric nanogenerators with output power density of 300 W m⁻², *Adv. Mater.* 32 (2020), <https://doi.org/10.1002/adma.202002824>.

- [30] M. Yuan, C.H. Li, H.M. Liu, Q.H. Xu, Y.N. Xie, A 3D-printed acoustic triboelectric nanogenerator for quarter-wavelength acoustic energy harvesting and self-powered edge sensing, *Nano Energy* 85 (2021), <https://doi.org/10.1016/j.nanoen.2021.105962>.
- [31] H.Y. Guo, et al., A highly sensitive, self-powered triboelectric auditory sensor for social robotics and hearing aids, *Sci. Robot.* 3 (2018), <https://doi.org/10.1126/scirobotics.aat2516>.
- [32] Jiang, Y. et al. Ultrathin Eardrum-Inspired Self-Powered Acoustic Sensor for Vocal Synchronization Recognition with the Assistance of Machine Learning. *Small*, doi: 10.1002/sml.202106960.
- [33] S. Kang, et al., Transparent and conductive nanomembranes with orthogonal silver nanowire arrays for skin-attachable loudspeakers and microphones, *Sci. Adv.* 4 (2018), <https://doi.org/10.1126/sciadv.aas8772>.
- [34] W. Yan, et al., Single fibre enables acoustic fabrics via nanometre-scale vibrations, *Nature* 603 (2022) 616–623, <https://doi.org/10.1038/s41586-022-04476-9>.
- [35] *Acoustic principle, Volume I*/Written by Cheng J.C. Second edition, Science Press, Beijing, 2019, p. 5.



Huake Yang received his B.S. degree in Applied Physics (2017) and M.S. degree in Physics (2020) from Chongqing University. Now, he is a Ph.D. student at Chongqing University. His research interests are mainly focused on nanogenerator.



Qianxi Yang received his B.S degree in Theoretical Physics from Chongqing University in 2020. Now he is a postgraduate student in Chongqing University. His current research focuses on triboelectric nanogenerator sensor.



Xiaochuan Li received his B.S. degree in Applied Physics from Chongqing University in 2019. Now, he is a PhD student in the field of physics, Chongqing University. His current research is triboelectric nanogenerators for energy harvesting.



Jun'an Lai received his B.S. degree in Functional Materials (2017) and M. S. degree in Materials Physics and Chemistry (2020) at Kunming University of Science and Technology. Now, he is a Ph. D. student in Optical Engineering at Chongqing University, his field of study is Optoelectronic functional materials and devices.



Yawen Hu received her B.S degree in Astronomy from China West Normal University in 2020. Now she is a postgraduate student in Chongqing University. Her current research focuses on triboelectric nanogenerator.



Qianying Li received her B.S. degree in Physics from Chongqing Technology and Business University in 2018. Now, she is a PhD student in the field of Physics, Chongqing University. Currently, her research interests are mainly focused on TENG-based high voltage technology.



Yi Xi is now a professor at Chongqing University, China. She received her PhD degree in Physics from Chongqing University in 2010. Her main research interests focus on the fields piezoelectric, triboelectric nanogenerators for energy harvesting and supercapacitors for energy storage, self-powered sensor system. She is the author of more than 150 publications and holds more than 10 patents.



Xuemei Zhang received her B.S. degree in physics from Chongqing Normal University in 2019. Now she is a post-graduate student in Chongqing University. Her current research is triboelectric nanogenerator.



Prof. Zhong Lin Wang received his PhD from Arizona State University in physics. He now is the Hightower Chair in Materials Science and Engineering, Regents' Professor, Engineering Distinguished Professor and Director, Center for Nanostructure Characterization, at Georgia Tech. Prof. Wang has made original and innovative contributions to the synthesis, discovery, characterization and understanding of fundamental physical properties of oxide nanobelts and nanowires, as well as applications of nanowires in energy sciences, electronics, optoelectronics and biological science. His discovery and breakthroughs in developing nanogenerators established the principle and technological road map for harvesting mechanical energy from environment and biological systems for powering a personal electronics. His research on self-powered nanosystems has inspired the worldwide effort in academia and industry for studying energy for micro-nano-systems, which is now a distinct disciplinary in energy research and future sensor networks. He coined and pioneered the field of piezotronics and piezo-phototronics by introducing piezoelectric potential gated charge transport process in fabricating new electronic and optoelectronic devices.